Chem

CellPress

Article

Molecular Memory Near Room Temperature in an Iron Polyanionic Complex

Andrea Moneo-Corcuera,[1] David Nieto-Castro,[1] Jordi Cirera,[2] Verónica Gómez,[1] Jesús Sanjosé-Orduna,[1] Carla Casadevall,[1] Gábor Molnár,[3] Azzedine Bousseksou,[3] Teodor Parella,[4] José María Martínez-Agudo,[5] Julio Lloret-Fillol,[1,6] Mónica Hevia Pérez-Temprano,[1]** Eliseo Ruiz,[2]** and José Ramón Galán-Mascarós[1,6,7]***

[1]Institute of Chemical Research of Catalonia (ICIQ), The Barcelona Institute of Science and Technology (BIST), Av. Països Catalans 16, 43007 Tarragona, Spain

[2]Departament de Química Inorgànica i Orgànica and Institut de Química Teòrica i Computacional, Universitat de Barcelona, Diagonal 645, 08028, Barcelona, Spain

[3]LCC, CNRS & University of Toulouse (UPS, INPT), 205 route de Narbonne, 31077 Toulouse, France

[4]Servei de Ressonància Magnètica Nuclear, Universitat Autònoma de Barcelona, 08193 Bellaterra Barcelona, Spain

[5]Instituto de Ciencia Molecular, Universidad de Valencia, Catedrático José Beltrán 2, 46980 Paterna, Spain

[6]ICREA, Passeig Lluís Companys, 23, 08010 Barcelona, Spain

[7]Lead contact

*Correspondence: mperez@iciq.es

**Correspondence: eliseo.ruiz@qi.ub.es

***Correspondence: jrgalan@iciq.es

SUMMARY

Bistable molecules represent a potential miniaturization limit for high-density information technologies. However, molecules exhibit memory effect typically at very low temperatures. This is the case of spin crossover (SCO) complexes, where the concept of a molecular memory has not been considered, due to the fast spin-state interconversion of all previous systems. Breaking this principle, here we report a slow relaxation process found in a SCO iron-triazole polyanionic complex. Multiple experimental evidences confirm the opening of a thermal hysteresis upon solid dilution and even in liquid solution. Density functional Theory (DFT) calculations assign the origin of this unexpected phenomenon to the appearance of an energy barrier that slows down the spin-state relaxation processes at the molecular level. These results show how SCO molecules may store information at room temperature, opening unique opportunities for molecular data storage.

Keywords: spin crossover, molecular memory, thermal hysteresis, DFT calculations, iron.

INTRODUCTION

Spin crossover materials are switchable transition metal complexes where the high spin (HS) and low spin (LS) states can be reversibly interconverted by external stimuli (temperature, light, pressure, magnetic field, etc.).[1-3] In the solid state these

The bigger picture

Single molecules are the smallest processable units for information storage and sensing. However, molecular phenomena is typically limited to very low temperatures. Thermal energy is able to depopulate (erase) the excited state back to the ground state. Spin crossover (SCO) molecules are an exception to this rule, showing memory effect above room temperature, but only when the electronic switchability is associated to a bulk phase transition. This synergy has its origin in the cooperativity among SCO molecules in the crystal, disappearing in diluted samples. We have found a surprising exception to this model: a polyanionic iron complex able to show memory effect even upon dilution. Our results demonstrate that molecular species can exhibit thermal hysteresis if intramolecular interactions are able to slow down the relaxation processes at the single molecule level. Our findings open unprecedented opportunities for single-molecule memories at (and above) room temperature.

complexes can show a thermal hysteresis loop, conferring a memory effect to the material – even at and above room temperature – as a result of cooperative intermolecular interactions (mainly of elastic origin) among a large ensemble of molecules.[4-11]

Several alternatives have been proposed to exploit SCO bistability at the nanoscale. SCO nanoparticles have shown to retain hysteresis down to a few nanometers. This miniaturization affects the temperature and width of the hysteresis cycle,[12-29] as confirmed by spatially resolved microscopy,[30-32] and by single-particle transport measurements.[33-42] Sensing applications were also investigated.[43]

Another strategy to achieve bistability in SCO molecules deals with the incorporation of bistable ligands, in the so-called "ligand driven spin state switching". In these cases, the isomerization of the ligands, typically induced by light, indirectly triggers the spin conversion.[44–47] This approach allows for memory effect at the molecular level due to electronic/ligand re-organization. However, the reversible photoswitching through ligand-driven effects is mostly limited to the liquid phase, though a few promising exceptions exist.[48–52]

The discovery of the light-induced excited spin state trapping (LIESST) effect in the 1980s generated great expectations for information storage and processing in SCO molecules.[53–57] However, this phenomenon is basically limited to cryogenic temperatures due to the small intramolecular barrier for the spin-state interconversion. This situation is similar to that of single-molecule magnets, struggling with low blocking temperatures.[58,59]

Here we demonstrate how a polyanionic iron trinuclear complex bridged by polysulphonated 1,2,4-triazole derivatives (Figure 1) exhibits memory effect upon dilution in a diamagnetic matrix, and even in liquid solution. These observations are unique for SCO materials, since thermal hysteresis was always attributed to cooperative effects arising from lattice interactions in the solid. In the absence of cooperativity, the memory effect in this system appears to have a pronounced molecular character, dominated by single-molecule events: intramolecular and/or supramolecular (with solvent molecules and surroundings). The twelve negatively charged sulfonate groups dominate and limit molecular dynamics. The LS⇔HS transitions with the different Fe–N bonding distances in each spin state configurations will require the corresponding reorganization of these anionic groups, with the surrounding cations and solvent molecules. These steric effects open an activation barrier resulting in extremely slow spin-state interconversion: several hours at room temperature.

RESULTS AND DISCUSSION

Magnetic solid dilutions

The $[Fe_3(\mu\text{-}L)_6(H_2O)_6]^{6-}$ polyanion (**Fe_3**, L = 4-(1,2,4-triazol-4-yl)ethanedisulfonate)[60] was diluted with its diamagnetic, isomorphous Zn^{II} analogue (**Zn_3**), given that their crystal structures with $(Me_2NH_2)^+$ cations are isostructural (Table S1 and Figure S1). The dilution series $(Me_2NH_2)_6[Zn_3(\mu\text{-}L)_6(H_2O)_6]_{(1-x)}[Fe_3(\mu\text{-}L)_6(H_2O)_6]_x$ (x = 1.00, 0.60, 0.40, 0.20 and 0.05) was obtained by fast precipitation of the corresponding mixed solutions of the two pure salts in the desired ratio (Methods sections and Table S2). ESEM-EDX mapping of the solid solutions showed homogeneous distribution of Fe and Zn (Table S3 and Figure S2). The absence of local phase separation was further confirmed by X-ray powder diffractograms (Figure S3) and their corresponding refined cell parameters (Figure S4 and S5). All plots are well fitted with the crystallographic data from the **Zn_3** single crystal solution. Interestingly, these materials show a slight contraction of the unit cell that corresponds to ≈3% for **Zn_3** and ≈ 4% for **5%Fe_3** (Tables S6-S7). No evidence of metal scrambling was detected in these solid dilutions by mass spectrometry and solution UV-Vis measurements during our fast precipitation

method (Figure S6 and S7). Thus, we can assume that the **Fe₃** and **Zn₃** trimers are the major polyanionic components of these solid solutions.

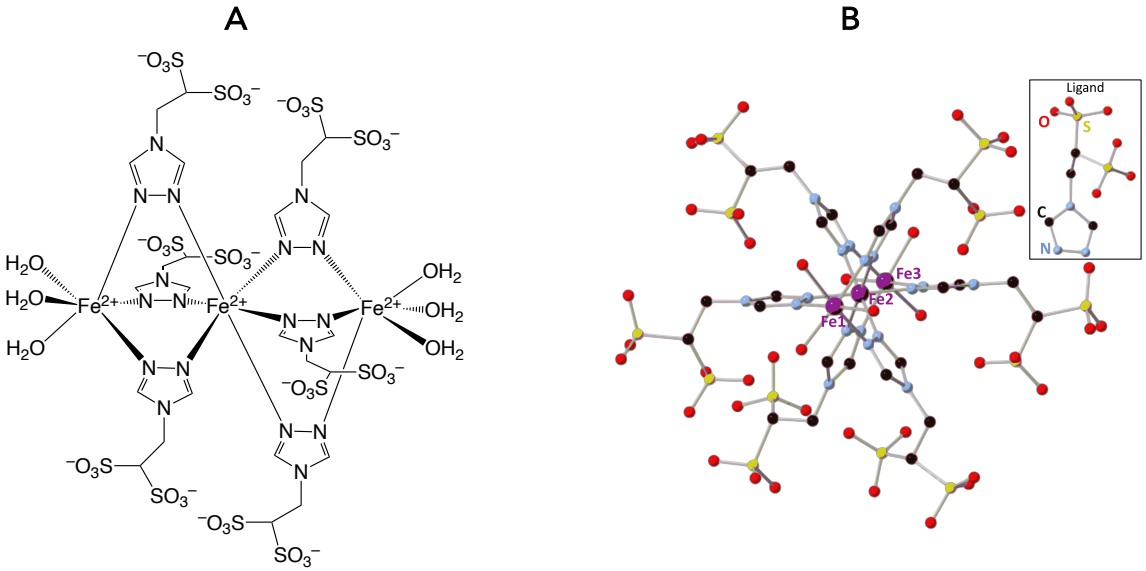

Figure 1. Molecular structure of the polyanionic FeII complex $[Fe_3(\mu\text{-}L)_6(H_2O)_6]^{6-}$(A) Scheme of the $[Fe_3(\mu\text{-}L)_6(H_2O)_6]^{6-}$ (L = 4-(1,2,4-triazol-4-yl)ethanedisulfonate) polyanion. (B) Molecular structure of the $[Fe_3(\mu\text{-}L)_6(H_2O)_6]^{6-}$ complex.

Magnetic susceptibility measurements were performed as a function of temperature. In the 2–300 K range, all samples show a typical paramagnetic behavior (Figure S8). At room temperature, the $\chi_m T$ value for **Fe₃** is 6.5 $cm^3mol^{-1}K$, consistent with a HS-LS-HS configuration in the Fe^{II} trimers (spin-only $\chi_m T$ = 6.0 $cm^3mol^{-1}K$).[60] The central Fe^{II} position remains in the LS state due to the strong ligand field imposed by the FeN_6 coordination to six triazole ligands. The terminal Fe positions remain in HS state down to 2 K, because three weak ligand field water molecules complete their coordination sphere. In the dilution series, the $\chi_m T$ values at room temperature are in good agreement with the corresponding **Fe₃** content (Table S4).

Upon heating over room temperature, at very slow scan rates (0.3 K min^{-1}) to avoid fast-scan artifacts,[61] the $\chi_m T$ product increases above 350 K corresponding to a gradual LS→HS transition on the central Fe, slowly reaching saturation after ≈ 8 hours at 400 K (Figure S9). The saturation values are consistent with a complete spin transition of the central Fe^{II} ion resulting in a HS-HS-HS trimer. It is worthy to mention that these solid solutions are thermally stable up to ≈ 500 K, as confirmed by thermogravimetric analyses (Figure S10). Thus, up to 400 K they only suffer dehydration (all magnetic measurements were performed with open capsules to avoid re-hydration processes). When the temperature is decreased, a thermal hysteresis appears. The HS-HS-HS state starts to be depopulated below ≈ 300 K, with a strong dependence on scan rate. For an easier comparison, the hysteresis cycles in Figure 2a are represented per mol of **Fe₃**, showing how dilution does not affect the width of the hysteresis cycle (Table S5 and Figure S11a). Main SCO parameters remain consistent within experimental error down to the highly diluted 5%-**Fe₃** sample with a 88 ± 6 K hysteresis width, $T_{1/2}\uparrow$ = 380 ± 5 K and $T_{1/2}\downarrow$ = 292 ± 6 K. Successive thermal cycles offer consistent magnetic behavior, discarding any contribution of a dehydration process to the magnetic measurements (Figure S11b).

According to common elastic models for spin crossover systems, the **Fe₃** thermal hysteresis should eventually disappear upon dilution in the **Zn₃** matrix. The bistability correlates with long-range cooperativity between SCO centers in the solid.[62–65] In addition, the spin transition temperatures should downshift due to the destabilization

of the smaller LS Fe^{II} moieties, given that the ionic radius of Fe^{II} in the HS state and Zn^{II} are nearly the same.[66] None of these expectations match the experimental data.

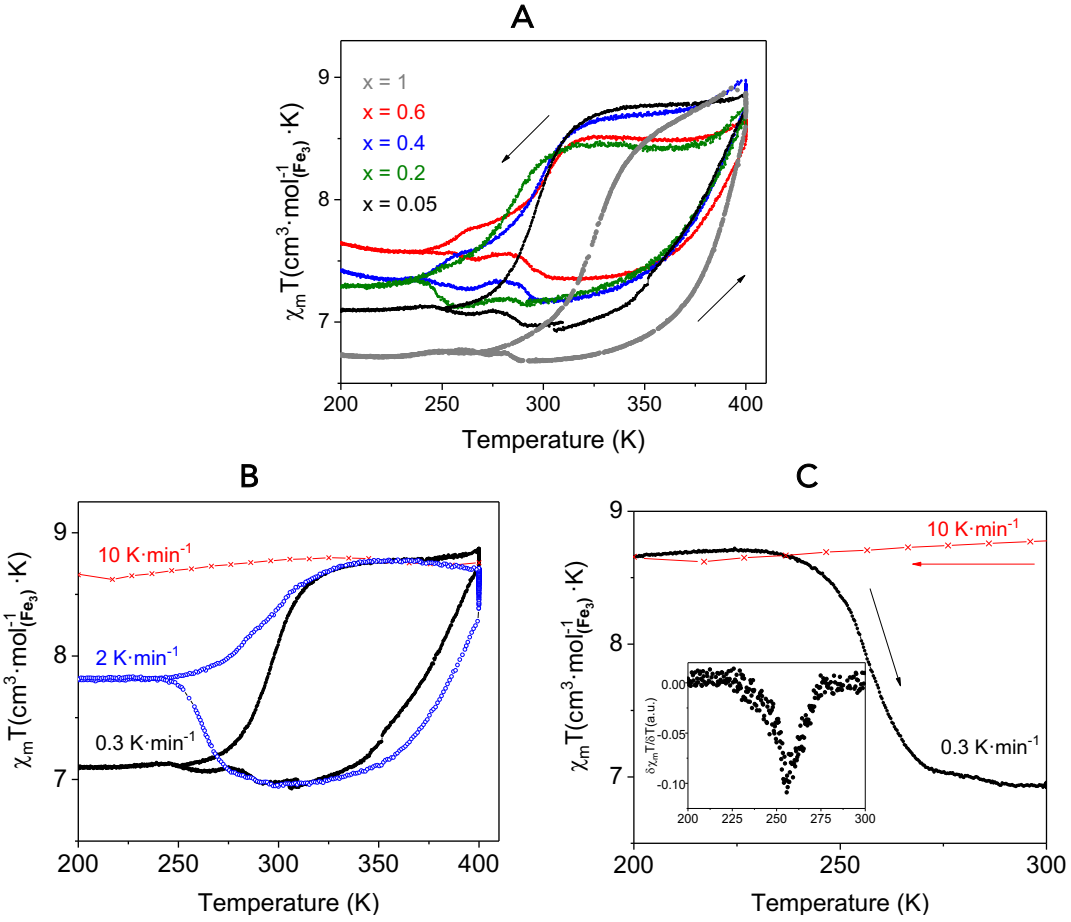

Figure 2. Spin crossover behavior of Fe3/Zn3 solid dilutions.

(A) Variable temperature magnetic data for the series $(Me_2NH_2)_6[Zn_3(\mu\text{-}L)_6(H_2O)_6]_{(1-x)}[Fe_3(\mu\text{-}L)_6(H_2O)_6]_x$ (x = 1.00, 0.60, 0.40, 0.20 and 0.05). Arrows indicate scan direction.

(B) Temperature dependence of the $\chi_m T$ product for $(Me_2NH_2)_6[Zn_3(\mu\text{-}L)_6(H_2O)_6]_{0.95}[Fe_3(\mu\text{-}L)_6(H_2O)_6]_{0.05}$ at different scan rates showing the trapping of metastable HS state when cooling down at >1 K min^{-1}.

(C) Determination of the T_{TIESST} from the heating branch (0.3 K min^{-1}) of the trapped HS state as cooled down at 10 K min^{-1}. For easier comparison, magnetic data is represented per mol of Fe^{II} trimer.

We studied in detail these kinetic effects in the $(Me_2NH_2)_6[Zn_3(\mu\text{-}L)_6(H_2O)_6]_{(1-x)}[Fe_3(\mu\text{-}L)_6(H_2O)_6]_x$ (x = 0.05, **5%Fe3**) solid solution (Figure 2b). While the heating branch shows almost identical behavior with scan rate, the cooling branch is highly scan-rate dependent, with the appearance of a trapping process at > 0.3 K min^{-1}. When the cooling scan rates are higher, the system cannot relax to the HS-LS-HS ground state and is trapped in its excited HS-HS-HS configuration, in a so-called "temperature-induced excited spin state trapping" (TIESST).[67] Over 40% of the HS-HS-HS species is quenched at a 2 K min^{-1} cooling rate, and > 90% is quenched at 10 K min^{-1}. Once the metastable state is trapped, the ground state can only be recovered by warming the sample above 250 K, which coincides with the estimated "TIESST temperature" (Figure 2c). This T_{TIESST} is similar in all dilutions to the bulk value (Figure S12). The relaxation curves of the trapped metastable HS-HS-HS state follow an exponential function below T_{TIESST}, and a stretched exponential function above T_{TIESST} (Figure S13a

and Equations S4 and S5). Both behaviors are typical for a non-cooperative system. The activation energy of the relaxation process has been estimated from the Arrhenius equation (Figure S13b and Equation S6) as E_a = 2015 ± 140 cm^{-1} (≈ 2900 K ≈ 5.8 kcal mol^{-1}). Remarkably, the relaxation process above 250 K becomes temperature-independent, as observed also in the pure compound **Fe_3**.

To rule out the participation of a crystallographic phase transition in the thermal hysteresis, we also investigated the structural evolution upon heating. We collected powder X-ray diffraction (PXRD) patterns for **Zn_3** and **5%Fe_3** as a function of temperature in vacuum to mimic the SQUID sample space conditions. Upon heating the samples from 298 K to 400 K, both compounds lose crystallinity with few broad peaks remaining at 400 K (Figure S14). No changes to the position or width of these peaks occur after cooling the samples back to room temperature (Figures S14) and these consistent spectra are maintained after successive cycles. Once these samples are left open to air at room temperature, the initial crystallinity is recovered. This confirms the molecular stability of the samples during these treatments (Figures S15). We also collected calorimetry data. In all cases we found that successive cycles are featureless after the initial heating ramp which is dominated by the dehydration process (Figure S16). All these data support again that no phase transition is taking place in the temperature range where the SCO thermal hysteresis is observed.

Thermal hysteresis in liquid solutions

As to further confirm the molecular origin of the observed memory effect, we decided to carry out experiments in liquid solution. The existence of the intact trimer in solution was supported by negative electrospray ionization mass spectroscopy. The mass spectra of an aqueous solution of **Fe_3** showed an abundant peak at *m/z* = 1768.55 that is assigned to $\{[Fe_3L_6](Na_3H_2)\}^-$ species (Figure S17).

The UV-vis absorption spectra for complex **Fe_3** (4 mM) dissolved in a water/ethylene glycol mixture shows a significant temperature-dependence in the absorbance around 320 nm (Figure S18). The **Fe_3** LS fraction can be directly related to the absorption intensity of this UV peak, since it is bleached at 293 K, suggesting that all Fe^{II} centers are HS at this temperature. Upon cooling to 243 K the absorption significantly increases, which denotes a conversion from the HS-HS-HS to the HS-LS-HS state. The heating process is quite abrupt, with a $T_{1/2}\uparrow$ = 270 K, whereas the cooling presents a more gradual character with a $T_{1/2}\downarrow$ = 256 K, thus opening a 14 K wide hysteresis. Both branches converge above 273 K closing the hysteresis loop and evidencing a complete and reversible spin state switching. This unexpected thermal hysteresis in liquid solution is reproducible with consistent parameters, as it appears to be scan rate independent in our accessible experimental range (Figure 3a, Figure S19). The relaxation process inside the hysteresis cycle is very slow, excluding the appearance of an experimental artefact related merely to slow thermalization. At *T* = 260 K, the **Fe_3** solution keeps a distinct spin state memory for over two hours (Figure 3b). No thermal effect was observed in the absorption spectra of analogous **Zn_3** solutions (Figure S7e), thus we can discard a solvation effect participating on the hysteretic behavior of the Fe_3 sample.

We collected solution NMR data in a mixture of D_2O/CD_3OD for the free ligand, and for **Zn_3** (Figure S20). The diamagnetic nature of Zn analogue allowed us to obtain 2D DOSY data (Figure S21a) that confirmed its symmetry and the absence of free ligand in solution. As expected, the NMR data for the Fe trimer at room temperature showed a much more complex spectroscopic scenario, due to the presence of paramagnetic species. We found a highly deshielded set of 1H signals with broad peaks around 23, 14 and 13 ppm. The paramagnetic nature of **Fe_3** hampered the collection of 2D DOSY data, resulting in very weak and broad signals (Figure S21b). In this case, the absence of free ligand in solution and of Zn/Fe metal scrambling were confirmed by comparative NMR spectra (Figure S22).

Next, we analyzed the behavior of $[Fe_3(\mu\text{-}L)_6(H_2O)_6]^{6-}$ in D_2O/CD_3OD solution as a function of temperature. Interestingly, at low temperatures, the intensity of the original set of signals decreases concurrently with the appearance of new peaks around 8.5, 4.8 and 4.4 ppm. Intuitively, the sharper shape of the new signals, and their position at higher magnetic fields allowed us to initially assign them to the HS-LS-HS trimer (denoted as H_{LS} signals).

Consequently, the original set of broader signals, predominant at room temperature, was assigned to the HS-HS-HS trimer (denoted as H_{HS} signals). The temperature-dependence between H_{HS} and H_{LS} in the ^{1}H-NMR spectra collected in the 250–300 K range (Figure 3c) demonstrates the existence in solution of a reversible, stable and dynamic chemical exchange process. Experimental evidence for this reversible equilibrium and signal assignments were collected from EXSY experiments (Figure S23–27). Any aggregate or nanoparticle formation can be discarded due to the good quality of the NMR data obtained, incompatible with the involvement of aggregated species in solution. This fact was also corroborated with dynamic light scattering (DLS) data, where no signal for species larger than the isolated trimers were found (Figure S28-S29).

As with UV-vis data, we can estimate the concentration of the HS-LS-HS species in solution to be proportional to the integral of the H_{LS} signals. The thermal evolution of the HS-LS-HS population (see integrals values in Figure S30) shows the appearance of a hysteresis, in agreement with the UV-vis data (Figure 3d). These findings support that both measurements follow the same equilibrium process between two molecular species in solution. It is important to remark that the thermal hysteresis observed in the liquid solution of **Fe$_3$** is analogous in water/ethylene glycol or water/methanol solution (Figure S31), and that the hysteresis observed by NMR is also consistent and repeatable in successive cycles (Figure S32–S33).

To further relate this thermal hysteresis observed in solution to a magnetic spin state switching, we carried out two additional magnetic susceptibility measurements. The NMR-based Evans method allows to estimate the total magnetic moment of a paramagnetic species in solution from the paramagnetic shift provoked in the reference solvent chemical shift. The results obtained for a solution of $(Me_2NH_2)_6[Fe_3(\mu\text{-}L)_6(H_2O)_6]$ are consistent with a reversible change in the spin state of the species in solution (See methods section, Figure 3e and Figure S34). The room temperature $\chi_m T$ product of ≈ 9.5 cm^3 K mol^{-1} indicates HS-HS-HS configuration, decreasing down to ≈ 6.8 cm^3 K mol^{-1} at 250 K, consistent with a dominant HS-LS-HS fraction, as observed in the solid-state data. The appearance of a thermal hysteresis, with a maximum width of ≈ 12 K is also evident when comparing the heating and cooling branches.

The magnetic susceptibility data of **Fe$_3$** liquid solutions were also recorded with a SQUID magnetometer (See Methods section). Despite the diamagnetic background of the blank solutions (solvents + glass tubing), and of an analogous **Zn$_3$** solution, the raw magnetization data confirms the appearance of a thermal hysteresis in the magnetic susceptibility (Figure 3f), that does not appear in any of the blanks (Figure S35). The cooling branch shows a higher paramagnetic signal than the heating branch, with a maximum width of ≈ 14 K.

The comparison of all spectroscopic and magnetic data obtained from different techniques on the liquid solutions of **Fe$_3$** (Figure S36) support the existence of a thermal hysteresis of the magnetic property in solution, where intermolecular long-range interactions are precluded. This point towards a molecular origin of the memory effect observed, controlled by the temperature–induced switching in the spin state of a single molecule.

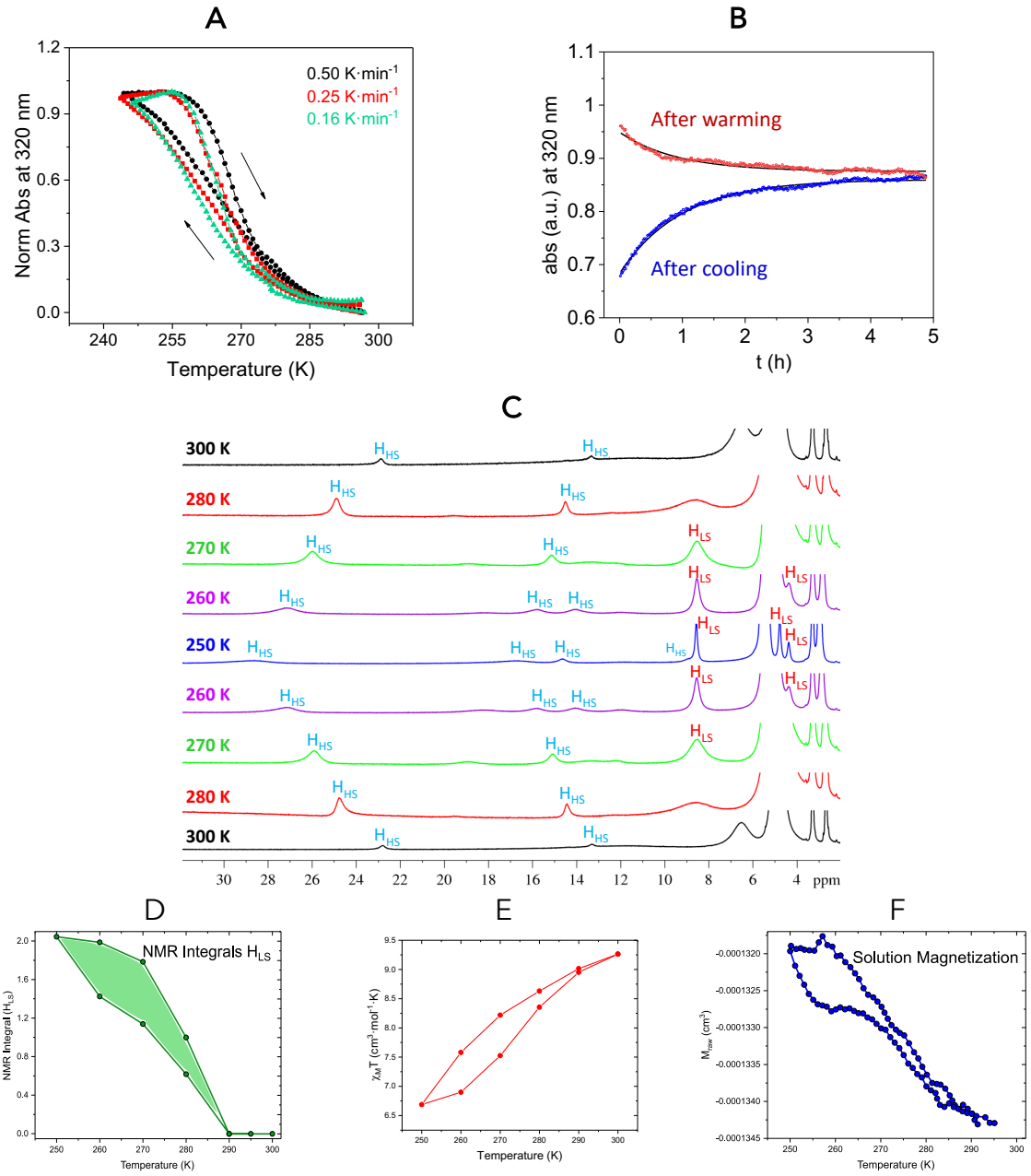

Figure 3. Spin crossover behavior of Fe3 in liquid solution.

(A) Thermal evolution of the normalized absorbance at 320 nm for an **Fe_3** solution (4 mM) in water/ethylene glycol (3:4) at different scan rates.

(B) Absorbance evolution in time at 260 K, after a cooling (blue points) or a warming process (red points) at 0.5 K min^{-1}. The isothermal curves are fitted with the simple exponential function, $Abs(t) = Abs_\infty + (Abs - Abs_\infty)\exp(-k_{HL} \cdot t)$, where the fitted parameters are Abs_∞ = 0.8601(4), $(Abs - Abs_\infty)$ = - 0.1763(9), k_{HL} = – 1.014(12) after cooling and Abs_∞ = 0.8753(4), $(Abs - Abs_\infty)$ = 0.0736(12), k_{HL}= –1.091(37) after warming.

(C) Evolution of the ^{1}H NMR spectra of **Fe_3** in D_2O/CD_3OD (3:4) in the 300–250 K range. The ^{1}H signals of the HS and LS species are defined as H_{HS} and H_{LS}, respectively.

(D) NMR H_{LS} peak integral at 8.5 ppm.

(E) Magnetic susceptibility estimated by Evans NMR spectroscopy.

(F) Magnetization data collected with a SQUID magnetometer.

Computational analyses on the origin of the SCO-based molecular memory

To shed light into the origin of this unexpected phenomenon, electronic structure calculations at the Density Functional Theory (DFT) level were done on the $[Fe_3(\mu\text{-}L)_6(H_2O)_6]^{6-}$ molecule. All calculations were done using the SCAN functional,[68] which has been recently benchmarked for several SCO systems with first row transition metal ions.[69] It provides a proper description of the ground states for all studied systems in this work (see Supplemental DFT calculations section). The theoretical analysis of the hysteresis in spin-crossover compounds using DFT methods was introduced by Wolny and co-workers using periodic and discrete models to study the effect of the spin state of nearest neighbors on the spin transition.[69,70] In that work, they introduce the energetic parameter H_{coop} as a measure to quantify the level of cooperativity in spin crossover systems from the effect of the surrounding metal centers upon the spin-state energy levels of a transitioning center (Figure 4A). H_{coop} is calculated as the difference found in the low- to high-spin transition energy of a transitioning center when surrounded by either high-spin cations, $E_1 = E$(HS-HS-HS) – E(HS-LS-HS), or low-spin cations, $E_2 = E$(LS-HS-LS) E(LS-LS-LS). The higher H_{coop}, the wider the thermal hysteresis expected in a material, as supported by the strong cooperativity in bulk. However, such parameter is ill-defined for a single molecule in which only one center undergoes spin-transition. The environment remains fixed, regardless of the spin-state. Here we propose a new analogous parameter, H_{block} (Figure 4B), that determines the relationship between the energies involved in the heating and cooling processes. For this trinuclear complex, the heating relates to E_1, quantified from HS-LS-HS to HS-HS-HS optimized geometries with a low-spin central center; and the cooling to E_2, quantified from the same HS-HS-HS to HS-LS-HS optimized geometries but with a HS central center. A positive value for H_{block} would indicate that higher energy is required in the cooling process than in the heating one (see SI for details). In other words, H_{block} can measure the structural quenching in SCO molecule to remain in a given spin-state. Even if both parameters (H_{coop} and H_{block}) refer to the thermodynamic contributions in a spin-transition process (kinetic effects have not been considered), a significant energy difference would predict longer relaxation times for one process compared to the other. Thus, this difference as estimated from H_{block}, can predict the possibility of a single SCO molecule to offer thermal hysteresis. H_{block} was computed for the fully optimized $[Fe_3(\mu\text{-}L)_6(H_2O)_6]^{6-}$ system, and also for an analogous complex in which the SO_3^- groups have been replaced by hydrogen atoms, noted as $[Fe_3(\mu\text{-}L')_6(H_2O)_6]^{6+}$ (see Supplemental DFT calculations section). An optimized model with eleven additional water molecules was studied to check the effect of the environment on the molecule (see details in Supplemental DFT calculations section). The corresponding values for the negative and positive isolated molecules are 6.0 and 2.4 kcal/mol, respectively while the value for the negative molecule with the water environment is 32.9 kcal/mol. It is remarkable to note that the computed H_{block} value for the isolated $[Fe_3(\mu\text{-}L)_6(H_2O)_6]^{6-}$ system is of the same order of magnitude than the corresponding H_{coop} parameter calculated for bulk systems showing thermal hysteresis due to intermolecular cooperative effects.[71] The inclusion of the external water molecules has a huge effect in the H_{block} parameter because it changes the conformation of the external ligands with SO_3^- groups and consequently, the electrostatic interaction between such SO_3^- groups and the Fe^{II} cations. As additional control calculations, we computed H_{block} for two Fe^{II} neutral complexes,[69] $[Fe(phen)_2(NCS)_2]$ and $[Fe\{H_2B(pz)_2\}_2(bipy)]$ (phen = phenantroline, bipy = bipyridine and $H_2B(pz)_2$ = dihydrogen bis(pyrazol-1-yl)borate), and in both cases H_{block} lays below 1 kcal/mol. These higher energy requirements found for negatively charged $[Fe_3(\mu\text{-}L)_6(H_2O)_6]^{6-}$ support the distinct observed behavior.

The origin this this phenomenon can be explained in the LS→HS transition of the central cation, which requires many significant changes in addition to Fe–N bond

lengths and magnetization increments. The estimated charge for the central Fe^{II} position in the HS state is also larger than in the LS state (around 0.4-0.5 e^-) due to the occupation of the antibonding e_g orbitals. This results in a net metal to ligand electron density transfer. The electrostatic interactions of the electro-deficient HS state with a negatively charged environment produces an overstabilization of the HS-HS-HS state. Thus, the high-spin state of the central cation is "blocked". This hinders the HS→LS cooling transition in such metal center (E_2 in a single-molecule process, Figure 4B) as it is shown experimentally in Figure 2 and 3, also in bulk phase with a very high T_{TIESST}.[60]

The inclusion of external water molecules in the calculations provokes that some SO_3^- groups interact with them instead of with terminal intramolecular hydrogen atoms. These water molecules (or other solvents able to generate hydrogen bond patterns) play a fundamental role in constraining the molecular geometry. These solvation effects help the SO_3^- groups to remain closer to the Fe^{II} cations, enhancing the electrostatic effects that stabilize the HS state of the central cation (see Supplemental Information, Table S8). In addition, the interactions between the charged SO_3^- groups with water molecules, and also with counter cations, will difficult the required structural changes in the coordination sphere of the central Fe^{II} cation as imposed by the spin transitions, that demand relatively large changes in the Fe–N bonds between both spin-states (see values in Supplemental section). Hence, there is a subtle dynamic balance of intermolecular and intramolecular hydrogen bond interactions, with the former enhancing the asymmetry (rigidity) between the heating-cooling processes.

If we consider a truthful single molecule in vacuum, as these calculations can do, we find a strong intramolecular H-bonding between the SO_3^- groups and the water molecules bound to the terminal Fe^{II} centers, that remain always in HS state (see Figure S37). The fixed spin of the terminal Fe^{II} centers creates a cage effect increasing the rigidity of the structure, and hindering the spin transition of the central iron. This is particularly relevant during the HS→LS transitions, that imply a size reduction, so yielding a "self-cooperative" effect, in addition to the more general electrostatic.

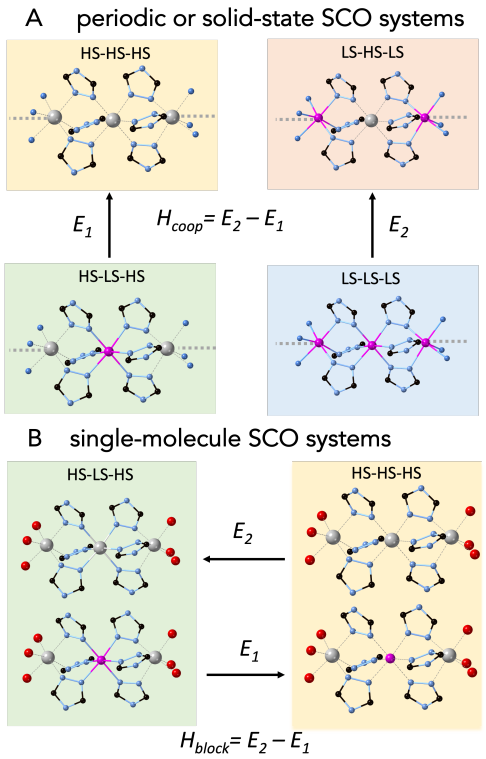

Figure 4. Description of the theoretical parameters that quantify the energy involved in the hysteresis processes in spin-crossover systems.

(A) H_{coop} determines the environmental influence if neighbor atoms are in the high (E_1) or low-spin (E_2) states in the spin-transition of a metal center. Consequently, a large H_{coop} value implies a high degree of cooperativity effects in periodic or solid-state systems.

(B) At single molecule level, there is no cooperativity, and H_{block} quantifies the difference between the structural quenching in the heating (E_1) and cooling (E_2) processes for the spin-transition of the central Fe^{II} metal ion.

Gray and purple spheres indicate HS and LS states respectively, while the label indicates the calculated structure. Dashed and normal bonds correspond to the distances of the HS and LS first coordination spheres to represent the larger coordination sphere of the LS structure.

CONCLUSION

During the last decades, one of the main challenges in molecular magnetism was to find a molecular magnetic material with open hysteresis at room temperature to realize molecular memory storage. Up to now, this research, based mainly in enhancing local magnetic anisotropy, has succeeded to reach a maximum temperature of 80 K with dysprosocenium molecules.[58,59] Here, we show that the challenge of molecular magnetic memories at high temperatures can be realized with spin crossover systems, even when bulk cooperativity was supposed to be an unavoidable requirement to exhibit thermal hysteresis.

A trinuclear iron complex exhibits thermal hysteresis in the transition between high- and low-spin states even upon dilution, where cooperative events are precluded. This phenomenon can be assigned to its constrained molecular structure, where charge distribution and anion-hydrogen bonding induce an over stabilization of the excited HS state, as confirmed by DFT analysis. As a result, the very slow relaxation down to

the LS ground state opens a thermal hysteresis, even in diluted liquid solution, demonstrating that SCO systems may also exhibit bistability at the single-molecule level.

It is important to mention the contribution of supramolecular interactions. Although the origin of the memory effect resides at the SCO polyanion, the over stabilization of the HS state will be tuned by the surroundings that may impose additional limitations to molecular restructuration. In general, these interactions are expected to enhance the memory effect. For instance, we found a > 90 K thermal hysteresis in solid dilutions, but a > 12 K thermal hysteresis in liquid solution, where molecular motion is less restricted.

EXPERIMENTAL PROCEDURES

Resource availability

Lead contact

Further information and requests for resources should be directed to and will be fulfilled by the lead contact, José Ramón Galán Mascarós (jrgalan@iciq.es).

Materials availability

All reagents were of commercial grade and used without further purification. The ligand 4-(1,2,4-triazol-4-yl)ethanedisulfonate (L) was obtained as the dimethylammonium salt $(Me_2NH_2)_2L$ following a literature procedure.[60]

Resource availability

Synthesis

$(Me_2NH_2)_6[Fe_3(\mu\text{-}L)_6(H_2O)_6]$ (**Fe_3**) was synthetized following a procedure reported previously in our group.[60] Single crystals were hand collected and used for all further experiments.

$(Me_2NH_2)_6[Zn_3(\mu\text{-}L)_6(H_2O)_6]$ (**Zn_3**)**.** $Zn(ClO_4)_2{\cdot}6H_2O$ (38 mg; 0.10 mmol), and $(Me_2NH_2)_2$**L** (90 mg; 0.24 mmol) were dissolved in water (5 mL total volume), obtaining a colorless solution. Ethanol vapor was slowly diffused into this aqueous solution to induce crystals growth. Single crystals of **Zn_3** were obtained after two days, filtered, washed with ethanol (3 × 15 mL) and dried in air.

$(Me_2NH_2)_6[Zn_3(\mu\text{-}L)_6(H_2O)_6]_{(1-x)}[Fe_3(\mu\text{-}L)_6(H_2O)_6]_x$ solid solutions. These diluted solid solutions were prepared from mixed aqueous solutions of **Fe_3** and **Zn_3** in the desired molar ratios (Table S2), with an excess of 2.5 equivalent of **L** (20 mg) in a total volume of 10 mL of water. Ascorbic acid was also added to avoid Fe^{II} oxidation. After 10 minutes stirring, the mixed samples were obtained by precipitation with ethanol (20 mL). This suspension was centrifuged to collect the solid and it was filtered and washed with ethanol/diethyl ether and dried in air. Yield: (37.2 mg) 63 % for *x* = 0.6; (38.7 mg) 64 % for *x* = 0.4; (40.1 mg) 65 % for x = 0.2; (43.5 mg) 54 % for x = 0.05. The actual Fe/Zn content was determined by EDX and ICP-OES analysis (Table S3). Still, the samples were labelled according to the initial ratio in the reagents.

Solutions of $(Me_2NH_2)_6[Fe_3(\mu\text{-}L)_6(H_2O)_6]$. **$Fe_3$** was dissolved in a mixture of water/ethylene glycol (4 mM) or water/methanol (1 mM) in a 3:4 volumetric ratio for both mixtures. The solutions were prepared and maintained under inert atmosphere to avoid the Fe^{II} oxidation. The aqueous mixtures, water/ethylene glycol and water/methanol mixtures (3:4) do not freeze at the lowest working temperature (≈ 240 K or ≈ –33^{0}C), having their freezing points around –50 and –65 ^{0}C, respectively (Figure S15a).

Instrumentation

ICP-OES was used to carry out elemental analysis with an Agilent 725-ES inductively coupled plasma optical emission spectrometer at University of Valladolid.

Environmental scanning electron microscopy (ESEM) images and Energy-dispersive X-ray spectroscopy (EDX) analysis were obtained with a QUANTA600 equipment (FI) under high vacuum conditions with a Large-Field Detector at 20 kV.

TGA was performed using a TGA/SDTA851 Mettler Toledo with a MT1 microbalance.

Dynamic light scattering (DLS) data was collected with a Malvern Nano ZS/ZEN3600.

X-ray powder diffraction (XRPD) measurements were made using a Siemens D5000 diffractometer fitted with a curved graphite diffracted-beam monochromator, incident and diffracted-beam Soller slits, a 0.06° receiving slit and scintillation counter as a detector. The angular 2**θ** diffraction range was between 5 and 40°. The data were collected with an angular step of 0.05° at 10s per step and sample rotation. Cu–k**α** radiation was obtained from a copper X-ray tube operated at 40 kV and 30 mA. The obtained XRPD patterns were analyzed by Pawley profile analysis using Topas software.[72]

High-resolution mass spectra (HRMS) were obtained with a MicroTOF II from Bruker Daltonics with the negative ionization mode (ESI^-). The instrument was operated at a capillary voltage of 4 kV with an end plate offset of –500 V, using N_2 as nebulizer gas at 0.4 bar and as dry gas at 4.0 L min^{-1} and a dry temperature of 180 °C. The instrument was calibrated with NaI clusters in the 876–2825 m/z range. The sample was introduced with direct injection with a syringe pump.

UV-vis spectra were recorded in 1 cm quartz cells with an Agilent 8453 diode array spectrophotometer (**λ** =190–1100 nm). A cryostat from Unisoku Scientific Instruments was used for temperature control. A Pt100 sensor was inserted into the quartz cell to monitor the exact temperature in the solution. The measurements were carried out under inert atmosphere.

NMR spectra were obtained on Bruker spectrometers (500 MHz and 600 MHz). ^1H NMR chemical shifts are reported in parts per million (ppm), relative to tetramethylsilane (TMS). The deuterated solvents were deoxygenated before their employment in the experiments. The relative integrals obtained in the subsequent thermal cycles of **Fe₃** were calculated using sodium 2,2-dimethyl-2-silapentane-5-sulfonate (DSS) as internal standard. All diffusion ^1H NMR experiments on the Zn compound were carried out on dilute solutions (concentration: 1 mM) at 250 K. All the spectroscopic data were processed, including the DOSY experiments, with the Bruker TOPSPIN software package. The paramagnetic susceptibility of solution of **Fe₃** was determined via the standard Evans measurements using ^1H-NMR spectroscopy. An NMR tube with a coaxial insert was used. The outer tube was filled with a 4 mM solution of **Fe₃** in D_2O/ethylene glycol (3:4) solution. To compensate the diamagnetic contribution of the ligands, the inner tube was filled with a 4 mM solution of diamagnetic zinc complex in D_2O/ethylene glycol. The concentration of the internal standard, non-deuterated acetone, was maintained constant in the inner and outer tubes (2% by volume). ^1H-NMR spectra were recorded in a 500 MHz spectrometer within the 250 – 300 K temperature range. Equation 1 was used to calculate the magnetic susceptibility from the experimentally measured shift in acetone signals between the inner and outer tubes.

$$\chi_m = \frac{3\delta f M}{4\pi f m} + \chi_m^0 + \frac{\chi_m^0(d_0 - d_x)}{m}\chi_{dia}^m \quad (1)$$

where χ_m is the molar paramagnetic susceptibility ($cm^3 \cdot mol^{-1}$), **δ**f is the frequency difference between the acetone peaks of the inner and outer tube (Hz), M the molecular weight of the paramagnetic complex ($g \cdot mol^{-1}$), f the frequency of the NMR instrument (Hz) and m the mass of the complex in 1mL of solution (g). χ_M^0 is the mass susceptibility of the solvent ($cm^3 \cdot mol^{-1}$), d_0 and d_x the density of the solvent and solution ($g \cdot cm^{-3}$) and $\chi_{dia}^m$is the diamagnetic correction ($cm^3 \cdot mol^{-1}$).

Since same solvents are used in the inner and outer tubes, the solvent correction factor (χ_m^0) could be neglected. Since the diamagnetic correction (χ_{dia}^m) in this experiment has been considered experimentally by using equivalent diamagnetic

complex in the inner tube, and same solvents are used in the inner and outer tubes, the solvent correction factor (χ_m^0), density difference and theoretical diamagnetic correction can be neglected. Thus, we use the Equation 2 for calculating the molar paramagnetic susceptibility.

$$\chi_m = \frac{3\delta f M}{4\pi f m} \quad (2)$$

Magnetic measurements were carried out on grained powders, placed in an open capsule, to allow dehydration during the first heating process, with a Quantum Design MPMS-XL SQUID magnetometer (Quantum Design, Inc, San Diego, CA, USA) under an applied field of 1000 Oe at different temperature scan rates. Experimental susceptibilities were corrected for the diamagnetic contribution. This contribution was experimentally obtained by fitting of the low temperature data (< 200 K) of each sample to a Curie-Weiss law with addition of a diamagnetic term:

$$\chi = \frac{C}{(T-\theta)} + \chi_{dia} \quad (3)$$

where χ is the magnetic susceptibility, C the Curie constant, T is temperature, θ is the Weiss constant and χ_{DIA} the diamagnetic contribution.

Solution magnetic measurements were carried with a Quantum Design MPMS-XL7 magnetometer equipped with the Reciprocating Sample Option (RSO) for higher sensitivity. The solutions were placed in the center of a 17 cm closed quartz tube and measured under a 1000 Oe magnetic field. The temperature program started at 300 K and the sample was cooled to 250 K and warmed again to 300 K at different cooling/heating rates to avoid spin trapping and thermal shift.

Single-crystal X-ray diffraction data of **Zn$_3$** were collected at 100(2) K on a Bruker APEX duo diffractometer with an APEX II CCD detector using Mo–K**α** (**λ**=0.71073 Å) and equipped with an Oxford Cryostrem 700 plus. Crystal structure solution was obtained using SIR2011 and refinement was performed using SHELX[73] v. 2018/3 under the ShelXle (Rev. 912) interface.[74] All non-hydrogen atoms were refined anisotropically. The asymmetric unit contains one molecule of the trimeric complex, six dimethyl ammonium cations and five crystallization water molecules (in addition to the six water molecules bound to Zn terminal cations). Most of the sulfonate rests of the polyanionic complex are disordered in two orientations. The dimethylammonium cations are disordered in 16 positions with different occupancies summing a total of six cations. The five crystallization water molecules are disordered in 13 positions with different occupancies. The structure was refined with strong damping factors based on the analogous isostructural iron derivative (CCDC 1016539) until, after some corrections and omitting the damping factors, it refined consistently. The measured sample was a weak diffracting crystal and only a ratio of 5.2:1 reflections to parameters was reached. The location of the cations and water molecules is extremely diffuse and their positions could only be located using the positions at the iron complex structure which was based on a much better dataset. Crystallographic data have been deposited at the Cambridge Crystallographic Database Centre, with deposition number CCDC 2019876. Copy of data can be obtained free of charge on application to the CCDC, Cambridge, UK via www.ccdc.cam.ac.uk/data_request/cif.

Powder X-ray diffraction (PXRD) measurements at 300 and 400 K were made using a Siemens D5000 diffractometer (Bragg−Brentano parafocusing geometry and vertical **θ**–**θ** goniometer) fitted with a curved graphite diffracted-beam monochromator, incident and diffracted-beam Soller slits, a 0.06° receiving slit, and a scintillation counter as a detector. The angular 2**θ** diffraction range was between 4° and 30°. The data were collected with an angular step of 0.05° at 10 s per step and sample rotation. A low background Si(510) wafer was used as sample holder. Cu-K**α** radiation was obtained from a copper X-ray tube operated at 40 kV and 30 mA. The obtained PXRD patterns were analyzed by Pawley profile analysis (between 4° and 30°) using the TOPAS software based on the Rietveld method.[75,76]

Computational methods

DFT calculations were performed by using the fhi-aims code.[77] The structures for high- and low-spin states were optimized with the PBE functional[78] using the tight numerical basis set (See Supplemental DFT calculations section).[77] Furthermore, dispersion effects were included by using the approach proposed by Tkatchenko and Scheffler.[79] GGA functionals provide very good optimised geometries in comparison with more sophisticated functionals (hybrid or meta GGA).[80] However, the GGA are not accurate to predict the energetics of the spin states because they result in a large overestimation of the stability of the low-spin state.[81] Hence, we have employed the SCAN meta-GGA functional developed by Perdew and coworkers[68] that some of us recently positively benchmarked with a large set of spin-crossover molecules.[69]

SUPPLEMENTAL INFORMATION

This section should include the titles and (optional) legends of all supplemental items. Document S1 is the main supplemental PDF:

ACKNOWLEDGMENTS

This work was supported by the European Union (projects ERC StG grant CHEMCOMP no 279313 and ERC CoG grant GREENLIGHT_REDCAT no 648304); the Ministerio de Ciencia e Innovación for support through Severo Ochoa Excellence Accreditation 2020-2023 (CEX2019-000925-S, MIC/AEI) and Maria de Maeztu Exellence Accreditation (MDM-2017-0767); the Spanish Ministerio de Ciencia e Innovación through the projects RTI2018-095618-B-I00, PGC2018-095808-B-I00, PGC2018-093863-B-C21 and CTQ2016-79942-P; the Generalitat de Catalunya (2017-SGR-1406 and 2017-SGR-1277), and the CERCA Programme/Generalitat de Catalunya. A.M.C. thanks MINECO for a predoctoral F.P.I. fellowship. J.C. thanks the Spanish MICINN for a Ramón y Cajal research contract (RYC2018-024692-I). J.S.-O. thanks Severo Ochoa Excellence Accreditation for a pre-doctoral contract. The Spanish Ministry of Science is acknowledged for a FPU (FPU014/02550) fellowship to C.C. We thank Jordi Benet-Buchholz and the X-ray Diffraction unit at ICIQ for their assistance in single crystal X-ray diffraction data collection and analysis. We thank Francesc Gispert-Guirado and the X-ray Diffraction Unit at URV for their assistance in powder X-ray diffraction data collection and analysis. We thank CSUC for computational resources.

AUTHOR CONTRIBUTIONS

J.R.G.M. proposed the concept. A.M.C., G.M., A.B., M.H.P.T. and J.R.G.M. designed the experiments. A.M.C., D.N.C. and V.G. performed the synthesis and characterization in the solid state. A.M.C., D.N.C., V.G. and J.M.M.A. carried out the magnetic susceptibility measurements. A.M.C., V.G., C.C. and J.L.F. performed the UV-vis spectroscopic measurements. A.M.C., J.S.O., M.H.P.T. and T.E. performed the NMR studies. J.C and E.R performed the computational calculations and derived theoretical models and conclusions. All authors participated in data analysis. A.M.C. and J.R.G.M wrote the paper with contributions from all authors.

DECLARATION OF INTERESTS

The authors declare no competing interests.

REFERENCES*

1. Bousseksou, A., Molnár, G., Salmon, L., Nicolazzi, W. (2011). Molecular spin crossover phenomenon: recent achievements and prospects. Chem. Soc. Rev. 40,

3313-3335. https://doi.org/10.1039/C1CS15042A

2. Gütlich, P., Hauser, A., Spiering, H. (1994). Thermal and optical switching of iron (II) complexes. Angew. Chem., Int. Ed. Engl. 33, 2024-2054. https://doi.org/10.1002/anie.199420241
3. Stock, P., Deck, E. Hohnstein, S., Korzekwa, J., Meyer, K., Heinemann, F.W., Breher, F., Hörner, G. (2016). Molecular spin crossover in slow motion: Light-induced spin-state transitions in trigonal prismatic iron (II) complexes. Inorg.Chem. 55, 5254-5265. https://doi.org/10.1021/acs.inorgchem.6b00238
4. Kahn, O., Martinez, C. J. (1998). Spin-transition polymers: from molecular materials toward memory devices. Science 279, 44-48. https://doi.org/10.1126/science.279.5347.44
5. Palii, A., Ostrovsky, S., Reu, O., Tsukerblat, B., Decurtins, S., Liu, S. X., Klokishner, S. (2015). Microscopic theory of cooperative spin crossover: Interaction of molecular modes with phonons. J. Chem. Phys. 143, 084502. https://doi.org/10.1063/1.4928642
6. Enachescu, A., Hauser, A. (2016) Study of switching in spin transition compounds within the mechanoelastic model with realistic parameters. Phys. Chem. Chem. Phys. 18, 20591–20599. https://doi.org/10.1039/C6CP02806C
7. Stoleriu, L., Nishimo, M., Miyashita, S., Stancu, A., Hauser, A., Enachescu, C. (2017). Cluster evolution in molecular three dimensional spin-crossover systems. Phys. Rev. B 96, 064115. https://doi.org/10.1103/PhysRevB.96.064115
8. Cruddas, J., Powell, B. J. (2019). Spin-state ice in elastically frustrated spin-crossver materials. J. Am. Chem. Soc. 141, 19790–19799. https://doi.org/10.1021/jacs.9b09191
9. Ohlrich, M., Powell, B. J. (2020). Fast, accurare enthalpy differences in spin crossover crystals from DFT+U. J. Chem. Phys. 153, 104107. https://doi.org/10.1063/5.0020706
10. Fouratti, H., Boukheddaden, K. (2020). Experimental evidences for the elastic long-range character of the spin crossover transition in cooperative single crystals. Phys. Rev. B 101, 224101. https://doi.org/10.1103/PhysRevB.101.224101
11. Popa, A., Stoleriu, L., Enachescu, C. (2021). Tutorial on the elastic theory of spin crossver materials. J. Appl. Phys. 129, 131101. https://doi.org/10.1063/5.0042788
12. Coronado, E., Galan-Mascaros, J. R., Monrabal-Capilla, M., García-Martínez, J., Pardo-Ibañez, P. (2007). Bistable spin - crossover nanoparticles showing magnetic thermal hysteresis near room temperature. Adv. Mater. 19, 1359-1361. https://doi.org/10.1002/adma.200700559
13. Galán-Mascarós, J. R., Coronado, E., Forment-Aliaga, A., Monrabal-Capilla, M., Pinilla-Cienfuegos, E., Ceolin, M. (2010). Tuning size and thermal hysteresis in bistable spin crossover nanoparticles. Inorg.Chem. 49, 5706-5714. https://doi.org/10.1021/ic100751a
14. Raza, Y., Volatron, F., Moldovan O. S., Ersen, O., Huc, V., Martini, C F. Brisset, A. Gloter, O. Stéphan, A. Bousseksou, L. Catala, T. Mallah. (2011). Matrix-dependent cooperativity in spin crossover Fe (pyrazine) Pt (CN) 4 nanoparticles. Chem. Commun. 47, 11501-11503. https://doi.org/10.1039/C1CC14463D
15. Peng, H., Tricard, S., Félix, G., Molnár, G., Nicolazzi, W., Salmon, L., Bousseksou, A. (2014). Re-appearance of cooperativity in ultra-small spin-crossover [Fe (pz){Ni (CN) 4}] nanoparticles. Angew. Chem. 126, 11074-11078. https://doi.org/10.1002/ange.201406710
16. Tanaka, D., Aketa, N., Tanaka, H. Tamaki, T., Inose, T., Akai, T., Toyama, H., Sakata, O., Tajiri, H., Ogawa, T. (2014). Thin films of spin-crossover coordination polymers with large thermal hysteresis loops prepared by nanoparticle spin coating. Chem. Commun. 50, 10074-10077. https://doi.org/10.1039/C4CC04123B
17. Slimani, A., Boukheddaden, K., Yamashita, K. (2014). Thermal spin transition of circularly shaped nanoparticles in a core-shell structure investigated with an electroelastic model. Phys. Rev. B, 89, 214109. https://doi.org/10.1103/PhysRevB.89.214109
18. Félix, G., Nicolazzi, W., Mikolasek, M., Molnár, G.,

Bousseksou, A. (2014). Non-extensivity of thermodynamics at the nanoscale in molecular spin crossover materials: a balance between surface and volume. Phys. Chem. Chem. Phys. 16, 7358-7367. https://doi.org/10.1039/C3CP55031A

19. Laisney, J., Tissot, A., Molnár, G., Rechignat, L., Rivière, E., Brisset, F., Bousseksou, A., Boillot. M. L. (2015). Nanocrystals of Fe (phen) 2 (NCS) 2 and the size-dependent spin-crossover characteristics. Dalton Trans. 44, 17302-17311. https://doi.org/10.1039/C5DT02840J

20. Giménez-Marqués, M., de Larrea, M. L. G. S., Coronado, E. (2015). Unravelling the chemical design of spin-crossover nanoparticles based on iron (II)–triazole coordination polymers: towards a control of the spin transition. J. Mater. Chem. C 3, 7946-7953. https://doi.org/10.1039/C5TC01093D

21. Feliz, G., Mikolasek, M., Peng, H. N., Nicolazzi, W., Molnar, G., Chumakov, A. I., Salmon, L., Bousseksou, A. (2015). Lattice dynamics in spin-crossover nanoparticles through nuclear inelastic scattering. Phys. Rev. B 91, 024422. https://doi.org/10.1103/PhysRevB.91.024422

22. Bartual-Murgui, C., Natividad, E., Roubeau, O. (2015). Critical assessment of the nature and properties of Fe (II) triazole-based spin-crossover nanoparticles. J. Mater. Chem. C 3, 7916-7924. https://doi.org/10.1039/C5TC01174D

23. Devid, E. J., Martinho, P. N., Kamalakar, M. V., Salitros, I., Prendergast, U., Dayen, J. F., Meded, V., Lemma, T., González-Pietro, R., Evers, F., Keyes, T. E., Ruben, M., Doudin, B., van der Molen, S. J. (2015). Spin transition in arrays of gold nanoparticles and spin crossover molecules. ACS Nano 9, 4496. https://doi.org/10.1021/acsnano.5b01103

24. Stoleriu, L., Stancu, A., Chakraborty, P., Hauser, A., Enachescu, C. (2015). Analysis of first order reversal curves in the thermal hysteresis of spin-crossover nanoparticles within the mechanoelastic model. Int. J. Appl. Phys. 117, 17B307. https://doi.org/10.1063/1.4914953

25. Linares, J., Jureschi, C. M., Boulmaali, A., Boukheddaden, K. (2016). Matrix and size effects on the appearance of the thermal hysteresis in 2D spin crossover nanoparticles. Phys. B: Condens. Matter 486, 164-168. https://doi.org/10.1016/j.physb.2015.09.048

26. Mikolasek, M., Nicolazzi, W., Terki, F., Molnár, G., Bousseksou, A. (2017). Surface transition in spin crossover nanoparticles. Chem. Phys. Lett. 678, 107-111. https://doi.org/10.1016/j.cplett.2017.04.031

27. Dugay, J., Evers, W., Torres-Cavanillas, R., Giménez-Marqués, M., Coronado, E., Van der Zant, H. S. (2018). Charge mobility and dynamics in spin-crossover nanoparticles studied by time-resolved microwave conductivity. J. Phys. Chem. Lett. 9, 5672-5678. https://doi.org/10.1021/acs.jpclett.8b02267.

28. Rubio-Giménez, V., Bartual-Murgui, C., Garbiati, M., Núñez-López, A., Castells-Gil, J., Quinard, B., Seneor, P., Otero, E., Ohresser, P., Cantarero, A., Coronado, E., Real, J. A., Mattana, R., Tatay, S., Martí-Gastaldo, C. (2o19). Chem. Sci., 10, 4038-4047. https://doi.org/10.1039/C8SC04935A

29. Usmani, S., Mikolasek, M., Gillet, A., Costa, J. S., Rigoulet, M., Chaudret, B., Bousseksou, A., Lassalle-Kaiser, B., Demont, P., Molnar, G. (2020). Spin crossover in Fe (triazole)–Pt nanoparticle self-assembly structured at the sub-5 nm scale. Nanoscale 12, 8180-8187. https://doi.org/10.1039/D0NR02154G

30. Van der Veen, R. M., Kwon, O. H., Tissot, A., Hauser, A., Zewail, A. H. (2013). Single-nanoparticle phase transitions visualized by four-dimensional electron microscopy. Nat. Chem. 5, 395-402. https://doi.org/10.1038/nchem.1622

31. Liu, S., Zhou, K., Yuan, T., Lei, W., Chen, H. Y., Wang, X., Wang, W. (2020). Imaging the thermal hysteresis of single spin-crossover nanoparticles. J. Am. Chem. Soc. 142, 15852-15859. https://doi.org/10.1021/jacs.0c05951

32. Hu, Y. W., Picher, M., Tran, N. M., Palluel, M., Stoleriu, L., Daro, N., Mornet, S., Enachescu, C., Freysz, E., Banhart, F., Chastanet, G. (2021). Photo-Thermal Switching of Individual Plasmonically Activated Spin Crossover Nanoparticle Imaged by Ultrafast Transmission Electron Microscopy. Adv. Mater. 33, 2105586. https://doi.org/10.1002/adma.202105586

33. Prins, F., Monrabal-Capilla, M., Osorio, E. A., Coronado, E., van der Zant, H. S. (2011). Room-

temperature electrical addressing of a bistable spin-crossover molecular system. Adv. Mater. 23, 1545-1549. https://doi.org/10.1002/adma.201003821

34. Dugay, J., Giménez-Marqués, M., Kozlova, T., Zandbergen, H. W., Coronado, E., van der Zant, H. S. (2015). Spin Switching in Electronic Devices Based on 2D Assemblies of Spin-Crossover Nanoparticles. Adv. Mater. 27, 1288-1293. https://doi.org/10.1002/adma.201404441
35. Holovchenko, A., Dugay, J., Giménez-Marqués, M., Torres-Cavanillas, R., Coronado, E., van der Zant, H. S. (2016). Near room-temperature memory devices based on hybrid spin-crossover@ SiO2 nanoparticles coupled to single-layer graphene nanoelectrodes. Adv. Mater. 28, 7228-7233. https://doi.org/10.1002/adma.201600890
36. Dugay, J., Aarts, M., Giménez-Marqués, M., Kozlova, T., Zandbergen, H. W., Coronado, E., Van Der Zant, H. S. J. (2017). Phase transitions in spin-crossover thin films probed by graphene transport measurements. Nano lett. 17, 186-193. https://doi.org/10.1021/acs.nanolett.6b03780
37. Salmon, L., Catala, L. (2018). Spin-crossover nanoparticles and nanocomposite materials. C. R. Chim. 21, 1230-1269. https://doi.org/10.1016/j.crci.2018.07.009
38. Polyzou, C. D., Malina, O., Tucek, J., Zboril, R., Panagiotou, N., Tasiopoulos, A. J., Boukos, N., Parthenios, J., Kalarakis, A. N., Tangoulis, V. (2019). Spin-Crossover Phenomenon in Microcrystals and Nanoparticles of a [Fe (2-mpz) 2Ni (CN) 4] Two-Dimensional Hofmann-Type Polymer: A Detailed Nano-Topographic Study. Inorg.Chem. 58, 13733-13736. https://doi.org/10.1021/acs.inorgchem.9b01405
39. Torres-Cavanillas, R., Lima-Moya, L., Tichelaar, F. D., Zandbergen, H. W., Giménez-Marqués, M., Coronado, E. (2019). Downsizing of robust Fe-triazole @ SiO 2 spin-crossover nanoparticles with ultrathin shells. Dalton Trans. 48, 15465-15469. https://doi.org/10.1039/C9DT02086A
40. Zhang, Y. T., Seguy, I., Ridier, K., Shalabaeva, V., Piedrhita-Bello, M., Rotaru, A., Salmon, L., Molnar, G., Bousseksou, A. (2020). Resistance switching in large-area vertical junctions of the molecular spin crossover complex [Fe (HB (tz) 3) 2]: ON/OFF ratios and device stability. J. Condens. Matter Phys., 32, 214010. https://doi.org/10.1088/1361-648X/ab741e
41. Sanchis-Gual, R., Torres-Cavanillas, R., Coronado-Puchau, M., Giménez-Marqués, M., Coronado, E. (2021). Plasmon-assisted spin transition in gold nanostar@ spin crossover heterostructures. J. Mater. Chem. C 9, 10811-10818. https://doi.org/10.1039/D1TC01943K
42. Torres.Cavanillas, R., Morant-Giner, M., Escorcia-Ariza, G., Dugay, J., Canet-Ferrer, J., Tatay, S., Cardona-Serra, S., Giménez-Marqués, M., Galbiati, M., Forment-Aliaga, A., Coronado, E. (2021). Spin-crossover nanoparticles anchored on MoS2 layers for heterostructures with tunable strain driven by thermal or light-induced spin switching. Nat. Chem. 13, 1101-1109. https://doi.org/10.1038/s41557-021-00795-y
43. Tsukiashi, A., Min, K. S. Kitayama, H., Teresawa, H., Yoshinaga, S., Takeda, M., Lindoy, L. F., Hayami, S. (2018). Sci. Rep., 8, 14911. https://doi.org/10.1038/s41598-018-33362-6
44. Khusniyarov, M. M. (2016). How to Switch Spin-Crossover Metal Complexes at Constant Room Temperature. Eur. J. Chem. 22, 15178-15191. https://doi.org/10.1002/chem.201601140
45. Boillot, M.L., Zarembowitch, J., Sour, A. (2004). Spin Crossover in Transition Metal Compounds II. Topics in Current Chemistry (Eds P. Gütlich, H.A. Goodwin) (Springer). https://doi.org/10.1021/ja040990e
46. Venkataramani, S., Jana, U., Dommaschk, M., Sönnichsen, F. D. Tuczek, F., Herges, R. (2011). Magnetic bistability of molecules in homogeneous solution at room temperature. Science, 331, 445-448. https://doi.org/10.1126/science.1201180
47. Witt, A., Heinemann, F. W., Khusniyarov, M. M. (2015). Bidirectional photoswitching of magnetic properties at room temperature: ligand-driven light-induced valence tautomerism. Chem. Sci. 6, 4599-4609. https://doi.org/10.1039/C5SC00130G
48. Hasegawa, Y., Takahashi, K., Kume, S., Nishihara, H. (2011). Complete solid state photoisomerization of bis (dipyrazolylstyrylpyridine) iron (II)

to change magnetic properties. Chem. Commun. 47, 6846-6848. https://doi.org/10.1039/C1CC11850A

49. Takahashi, K., Hasegawa, Y., Sakamoto, R., Nishikawa, M., Kume, S., Nishibori, E., Nishihara, H. (2012). Solid-state ligand-driven light-induced spin change at ambient temperatures in bis (dipyrazolylstyrylpyridine) iron (II) complexes. Inorg. Chem. 51, 5188-5198. https://doi.org/10.1021/ic300030b
50. Tissot, A., Boillot, M. L., Pillet, S., Codjovi, E., Boukheddaden, K., Lawson Daku, L.M. (2010). Unidirectional Photoisomerization of Styrylpyridine for Switching the Magnetic Behavior of an Iron(II) Complex: A MLCT Pathway in Crystalline Solids. J. Phys. Chem. C 114, 21715-21722. https://doi.org/10.1021/jp106583f
51. Rösner, B., Milek, M., Witt, A., Gobaut, B., Torelli, P., Fink, R. H. Khusniyarov, M. M. (2015). Reversible Photoswitching of a Spin - Crossover Molecular Complex in the Solid State at Room Temperature. Angew. Chem. Int. Ed. 54, 12976-13172. https://doi.org/10.1002/ange.201504192
52. Poggini, L., Milek, M., Londi, G., Naim, A., Poneti, G., Squillantini, L., Magnani, A., Totti, F., Rosa, P., Khusniyarov, M. M., Mannini, M. (2018). Room temperature control of spin states in a thin film of a photochromic iron (II) complex. Mater. Horizons 5, 506-513. https://doi.org/10.1039/C7MH01042G
53. Ohkoshi, S. I., Imoto, K., Tsunobuchi, Y., Takano, S., Tokoro, H. (2011). Light-induced spin-crossover magnet. Nat. Chem 3, 564-569. https://doi.org/10.1038/nchem.1067
54. Marino, A., Chakraborty, P., Servol, M., Lorenc, M., Collet, E., Hauser, A. (2014). The Role of Ligand - Field States in the Ultrafast Photophysical Cycle of the Prototypical Iron(II) Spin - Crossover Compound [Fe(ptz)6](BF4)2 Angew. Chem. Int. Ed. 53, 3863-38667. https://doi.org/10.1002/anie.201310884
55. Létard, J. F., Guionneau, P., Nguyen, O., Costa, J.S., Marcén, S., Chastanet, G. Marchivie, M., Goux-Capes, L. (2005). A guideline to the design of molecular - based materials with long - lived photomagnetic lifetimes. Chem. Eur. J. 11, 4582-4589. https://doi.org/10.1002/chem.200500112
56. Wu, C. C., Jung, J., Gantzel, P. K., Gütlich, P., Hendrickson, D. N. (1997). LIESST effect studies of Iron (II) spin-crossover complexes with phosphine ligands: Relaxation kinetics and effects of solvent molecules. Inorg. Chem. 36, 5339-5347. 1997, 36, 5339. https://doi.org/10.1021/ic9700359
57. Decurtins, S., Gütlich, P., Köhler, C. P., Spiering, H., Hauser, A. (1984). Light-induced excited spin state trapping in a transition-metal complex: The hexa-1-propyltetrazole-iron (II) tetrafluoroborate spin-crossover system. Chem. Phys. Lett. 105, 1-4. 1984, 105, 1. https://doi.org/10.1016/0009-2614(84)80403-0
58. Goodwin, C. A., Ortu, F., Reta, D., Chilton, N. F., Mills, D. P. (2017). Molecular magnetic hysteresis at 60 kelvin in dysprosocenium. Nature 548, 439-442. https://doi.org/10.1038/nature23447
59. Guo, F. S., Day, B. M., Chen, Y. C., Tong, M. L., Mansikkamäki, A., Layfield, R. A. (2018). Magnetic hysteresis up to 80 kelvin in a dysprosium metallocene single-molecule magnet. Science 362, 1400-1403. https://doi.org/10.1126/science.aav0652
60. Gómez, V., Saenz de Pipaon, C., Maldonado-Illescas, P., Waerenborgh, J. C., Martin, E., Benet-Buchholz, J., Galán-Mascarós, J. R. (2015). Easy excited-state trapping and record high T_{TIESST} in a spin-crossover polyanionic FeII trimer. J. Am. Chem. Soc. 137, 11924-11927. 2015, 137, 11924. https://doi.org/10.1021/jacs.5b07879
61. Brooker, S. (2015). Spin crossover with thermal hysteresis: Practicalities and lessons learnt. Chem. Soc. Rev. 44, 2880-2892. 2015, 44, 2880. https://doi.org/10.1039/C4CS00376D
62. Balde, C., Desplanches, C., Le Gac, F., Guionneau, P., Létard, J. F. (2014). The role of iron (II) dilution in the magnetic and photomagnetic properties of the series [Fe x Zn 1− x (bpp) 2](NCSe) 2. Dalt. Trans. 43, 7820-7829. https://doi.org/10.1039/C3DT52964A
63. Paradis, N., Chastanet, G., Létard, J. F. (2012). When stable and metastable HS states meet in spin-crossover compounds.

Eur. J. Inorg. Chem. Eur. J. Inorg. Chem. 2012, 3618-3624. https://doi.org/10.1002/ejic.201200297

64. Ganguli, P., Guetlich, P. +., Mueller, E. (1982). Effect of metal dilution on the spin-crossover behavior in [FexM1-x (phen) 2 (NCS) 2](M= Mn, Co, Ni, Zn). Inorg. Chem. 21, 3429-3433. https://doi.org/10.1021/ic00139a032
65. Martin, J. P., Zarembowitch, J., Dworkin, A., Haasnoot, J. G., Codjovi, E. (1994). Solid-state effects in spin transitions: influence of iron (II) dilution on the magnetic and calorimetric properties of the series [FexNi1-x (4, 4'-bis (1, 2, 4-triazole)) 2 (NCS) 2]. cntdot. H2O. Inorg. Chem. 33, 2617-2623. https://doi.org/10.1021/ic00090a023
66. Hauser, A., Enachescu, C., Daku, M. L., Vargas, A., Amstutz, N. (2006). Low-temperature lifetimes of metastable high-spin states in spin-crossover and in low-spin iron (II) compounds: The rule and exceptions to the rule. Coord. Chem. Rev. 250, 1642-1652. https://doi.org/10.1016/j.ccr.2005.12.006
67. Marchivie, M., Guionneau, P., Létard, J. F., Chasseau, D., Howard, J. A. (2004). Thermal trapped iron (II) high spin state investigated by X-ray diffraction. J. Phys. Chem. Solids 65, 17-23. https://doi.org/10.1016/j.jpcs.2003.09.002
68. Sun, J., Ruzsinszky, A., Perdew, J. P. (2015). Strongly constrained and appropriately normed semilocal density functional. Phys. Rev. Lett. 115, 036402. https://doi.org/10.1103/PhysRevLett.115.036402
69. Cirera, J., Ruiz, E. (2020). Assessment of the SCAN Functional for Spin-State Energies in Spin-Crossover Systems. The J. Phys. Chem. A 124, 5053-5058. https://doi.org/10.1021/acs.jpca.0c03758
70. Rackwitz, S., Klopper, W., Schünemann, V., Wolny, J. A. (2013). Quantification of intramolecular cooperativity in polynuclear spin crossover Fe (II) complexes by density functional theory calculations. Phys. Chem. Chem. Phys 15, 15450-15458. https://doi.org/10.1039/C3CP52240G
71. Wolny, J. A., Hochdörffer, T., Sadashivaiah, S., Auerbach, H., Jenni, K., Scherthan, L., Li, A.M., von Malotki, C., Wille, H.C., Schünemann, V. (2020). Vibrational properties of 1D-and 3D polynuclear spin crossover Fe (II) urea-triazoles polymer chains and quantification of intrachain cooperativity J. Phys.: Cond. Matter. 33(3), 034004. https://doi.org/ 10.1088/1361-648X/aba71d
72. Coelho, A. A., Evans, J., Evans, I., Kern, A., Parsons, S. (2011). The TOPAS symbolic computation system. Powder Diffr. 26, S22-S25. https://doi.org/10.1154/1.3661087
73. Sheldrick, G. M. (2015). Crystal structure refinement with SHELXL. Acta Cryst. C. 71, 3-8. https://doi.org/10.1107/S2053229614024218
74. Hübschle, C. B., Sheldrick, G. M.,Dittrich, B. (2011). ShelXle: a Qt graphical user interface for SHELXL. J. Appl. Cryst. 44, 1281-1284. https://doi.org/10.1107/S0021889811043202
75. Blum, V., Gehrke, R., Hanke, F., Havu, P., Havu, V., Ren, X., Scheffler, M. (2009). Ab initio molecular simulations with numeric atom-centered orbitals. Comput. Phys. Commun. 180, 2175-2196. https://doi.org/10.1016/j.cpc.2009.06.022
76. Rietveld, H. M. (1967). Line profiles of neutron powder-diffraction peaks for structure refinement. Acta Cryst. 22, 151-152. https://doi.org/10.1107/S0365110X67000234
77. Scardi, P., Azanza Ricardo, C. L., Perez-Demydenko, C., Coelho, A. A. (2018). Whole powder pattern modelling macros for TOPAS. J. Appl. Cryst. 51, 1752-1765. https://doi.org/10.1107/S160057671801289X
78. Perdew, J. P., Burke, K., Ernzerhof, M. (1996). Generalized gradient approximation made simple. Phys. Rev. Lett. 77, 3865. 1996, 77, 3865. https://doi.org/10.1103/PhysRevLett.77.3865
79. Tkatchenko, A., Scheffler, M. (2009). Accurate molecular van der Waals interactions from ground-state electron density and free-atom reference data. Phys. Rev. Lett. 102, 073005. https://doi.org/10.1103/PhysRevLett.102.073005
80. Bühl, M., Kabrede, H. (2006). Geometries of transition-metal complexes from density-functional theory. J. Chem. Theory Comput. 2, 1282-1290. 2006, 2, 1282. https://doi.org/0.1021/ct6001187

81. Cirera, J., Via-Nadal, M., Ruiz, E. (2018). Benchmarking density functional methods for calculation of state energies of first row spin-crossover molecules. Inorg.chem. 57, 14097-14105. https://doi.org/10.1021/acs.inorgchem.8b01821